Dimensionality effect on surface states and piezoelectric behavior in ZnO nanowires grown by pulsed-liquid injection metal–organic chemical vapor deposition

Lisa Legardinier, Gustavo Ardila, Quang Chieu Bui, Isabelle Gélard, Carmen Jiménez, Thomas Jalabert, Manuel Manrique, Bassem Salem, Sébastien Labau, Matthieu Weber, et al.

To cite this version:

Lisa Legardinier, Gustavo Ardila, Quang Chieu Bui, Isabelle Gélard, Carmen Jiménez, et al.. Dimensionality effect on surface states and piezoelectric behavior in ZnO nanowires grown by pulsed-liquid injection metal–organic chemical vapor deposition. ACS Applied Electronic Materials, 2024, 6 (9), pp.6344-6355. ⟨10.1021/acsaelm.4c00549⟩. ⟨hal-04710640⟩

HAL Id: hal-04710640

https://hal.science/hal-04710640v1

Submitted on 26 Sep 2024

Dimensionality Effect on Surface States and Piezoelectric Behavior in ZnO Nanowires Grown by Pulsed-Liquid Injection Metal-Organic Chemical Vapor Deposition

Lisa Legardinier[1,2], Gustavo Ardila[2*], Quang Chieu Bui[1,2,3], Isabelle Gélard[1], Carmen Jimenez[1], Thomas Jalabert[2], Manuel Manrique[1,3], Bassem Salem[3], Sébastien Labau[3], Matthieu Weber[1], Fabrice Donatini[4], and Vincent Consonni[1*]

[1]Université Grenoble Alpes, CNRS, Grenoble INP, LMGP, F-38000 Grenoble, France
[2]Université Grenoble Alpes, Univ. Savoie Mont Blanc, CNRS, Grenoble INP, CROMA, F-38000 Grenoble, France
[3]Université Grenoble Alpes, CNRS, CEA-LETI, Grenoble INP, LTM, F-38054 Grenoble, France
[4]Université Grenoble Alpes, CNRS, Grenoble INP, Institut Néel, F-38000 Grenoble, France

Abstract

ZnO nanowires are known as promising candidates for the development of highly efficient mechanical energy transducers using biocompatible and non-critical materials. However, the critical decoupling of the different contributions to the piezoelectric response of ZnO nanowires coming from the dimensionality effect, the nature and amount of defects, the density of free charge carriers, as well as the nature and density of surface traps is still lacking. The growing attractivity of mechanical energy transducers thus necessitates a thorough study on the interplay among piezoelectricity process, free charge carrier screening and surface depletion effects in these semiconducting nanowires, as well as their relationship to the dimensions of ZnO nanowires. To this day, the growth of ZnO nanowires by pulsed-liquid injection metal-organic chemical vapor deposition has been less explored despite the excellent structural and optical properties of ZnO nanowires. By fixing all growth conditions except for the growth time, the impact of the dimensions of ZnO nanowires on their piezoelectric and physical properties is carefully assessed. Based on electrical characterization and cathodoluminescence measurements, the densities of free electrons and of surface traps are determined in the ranges of 1.8 – 3.3 x 10^{18} cm^{-3} and 5 x 10^{12} to 1 x 10^{13} cm^{-2}, respectively, and are shown to vary with the radius of ZnO nanowires. The introduction of Al_{Zn} and carbon species in ZnO nanowires are further responsible for their high electrical conductivity. Furthermore, the piezoelectric response of ZnO nanowires is experimentally determined by piezoresponse force microscopy and compared with theoretical expectations based on finite element method simulation, showing that the piezoelectric coefficient in the range of 4.5 to 5.5 pm/V strongly depends on the dimensions of ZnO nanowires as an ultimate tool to enhance the performance of the related mechanical energy transducers.

Keywords: piezoelectricity, ZnO nanowires, dimensionality, metal-organic chemical vapor deposition, finite element method

Corresponding Authors: gustavo.ardila@grenoble-inp.fr and vincent.consonni@grenoble-inp.fr

1. Introduction

As an abundant and biocompatible semiconductor material, zinc oxide (ZnO) has extensively been utilized in numerous piezoelectric devices, particularly in their nanowire (NW) form, which has demonstrated promising outcomes in nanogenerator and strain/stress sensor applications.[1–5] Furthermore, the use of individual ZnO NWs as field-effect transistors (FET) or diodes, using the piezotronic effect, has been developed with promising results.[6–9] Diverse growth techniques can be employed to grow ZnO NWs, from wet chemical methods like chemical bath deposition,[4,10,11] to metal-organic chemical vapor deposition (MOCVD).[12–15] This latter approach is recognized as an interesting chemical method for achieving rapid NW growth over a large surface area while maintaining excellent structural and optical properties. Nonetheless, optimizing the growth process necessitates extensive exploration of numerous parameters, including the growth temperature,[16] the chemical precursor nature[17] or the flow rates.[18] While thermal evaporation and chemical bath deposition have widely been employed for depositing ZnO in various forms for piezoelectric devices,[11,19–21] the utilization of the MOCVD process has been relatively limited in this context. In addition, most studies have focused on using an MOCVD reactor with a bubbler system for growing ZnO thin films and NWs.[22–24] The pulsed-liquid injection MOCVD (PLI-MOCVD) process occurs to be advantageous due to its ability to mix the zinc chemical precursor in a solvent and operate at lower growth temperatures, making it a highly appealing alternative.[15,25,26]

Only a few studies have investigated the correlation between the piezoelectric and electrical properties in vertically-aligned ZnO NWs. Scrymgeour et al. demonstrated a clear relationship between the electrical resistivity and piezoelectric response of individual ZnO nanorods, showing the increase of the piezoelectric performance as the electrical resistivity is increased. Other reports have investigated the influence of the diameter,[27] growth conditions,[28] substrate,[26] or doping[29] on the piezoelectric performance of ZnO NWs. The dimensionality effect on ZnO NWs holds significant importance, particularly in relation to their piezoelectric properties and to the influence of surface traps and free charge carriers. The unique geometry of ZnO NWs, characterized by their high aspect ratio and large surface-to-volume ratio, imparts distinctive properties compared to bulk materials. The presence of surface traps, such as oxygen molecules, plays a crucial role in the piezoelectric response of NWs. These traps capture free charge carriers from the NW core, resulting in a modified distribution of free charge carriers along the NW surface. This leads to the formation of a depletion region with a low electrical conductivity and a bending in the energy band structure near the surface. As a consequence, the piezoelectric potential screening, caused by the compensation of generated free charge carriers, is influenced by the density of surface traps.[30] Moreover, the density of free charge carriers within the NWs also plays a vital role in their piezoelectric behavior. The surface traps and free charge carriers collectively contribute in an intricate manner to the overall piezoelectric response of ZnO NWs,[31] making the dimensionality effect a crucial consideration for optimizing and understanding their piezoelectric performance in various applications.[27,28,32] Nevertheless, the decoupling of the different contributions to the piezoelectric response of ZnO NWs originating from the dimensionality effect, the nature of defects, the density of free charge carriers, as well as the nature and density of surface traps, has, until now, not experimentally been investigated in detail.

In this work, the effect of various dimensions of ZnO NWs grown by PLI-MOCVD on their piezoelectric and physical properties is thoroughly investigated. By varying the deposition time, the radius, length and density of ZnO NWs are tuned over a broad range of values, as characterized by scanning electron microscopy (SEM) and atomic force microscopy (AFM). The electrical properties of single ZnO NWs are determined by four-point probe resistivity measurements combined with tunneling atomic force microscopy (TUNA), giving a first approximation of the density of free charge carriers as supported by a qualitative comparison with the literature. The nature and amount of defects in the bulk of ZnO NWs are studied by low-temperature cathodoluminescence (CL) spectroscopy coupled with Raman spectroscopy, while their nature and amount on the surfaces of ZnO NWs are assessed by time-resolved CL spectroscopy combined with X-ray photoelectron spectroscopy (XPS). This shows a strong correlation between the dimensions of ZnO NWs and the density of surface traps and free charge carriers. The piezoelectric properties of ZnO NWs are further investigated by piezoresponse force microscopy (PFM) supported by finite element method (FEM) calculations, carefully highlighting and decoupling the different contributions originating from the dimensions of ZnO NWs as well as from their electrical and surface properties to their piezoelectric response.

2. Experimental and theoretical procedures

ZnO nanowire growth. ZnO NWs were grown by PLI-MOCVD, with an Annealsys MC-200 reactor, on heavily p-type doped Si (100) substrates. A diethylzinc (DEZn, $Zn(C_2H_5)_2$) liquid solution was used as precursor. To that extent, a 100 mL DEZn solution with a 1 M concentration was diluted in cyclohexane (C_6H_{12}), leading to a concentration of 0.43 M. The diluted DEZn solution was injected inside the chamber of the reactor at a liquid flow rate of 0.5 g/min and with an Ar carrier gas flow rate of 500 sccm. The O_2 gas was set to a 300 sccm flow rate, corresponding to a O/Zn ratio of 48. During the growth process, the pressure inside the chamber was kept at 3 mbar. The substrate was heated at a temperature of 700 °C and a rotation of 30 rpm was performed to ensure the homogeneity. The growth time was varied from 3 minutes to 1 hour.

Electrical property measurements. After being dispersed on a Si_3N_4-coated Si substrate, a single NW was contacted with four metallic electrodes assisted by electron-beam lithography, Au and Ti vacuum deposition and lift-off process. The current-voltage (*I-V*) measurements were performed with *in situ* SEM four-probe nanomanipulators, using the electron beam to deplete the NW surface with a dose of 4×10^5 µC/cm^2. TUNA measurements were performed with a Bruker Dimension Icon atomic force microscope (AFM). Platinum-coated silicon tips (PtSi-NCH from Brucker) characterized by a spring constant ranging from 30 to 50 Nm^{-1} and a resonance frequency between 204 and 497 kHz were used. The measure precision was tested beforehand with a 10 kΩ resistance. The heavily p-type doped Si (100) substrates served as the bottom electrodes. A bias voltage was applied between the conductive tip and the substrate in the range of -5 V to 5 V, and the current was detected while passing through the sample with a sensitivity of 100 nA/V. Mapping images were collected through the DataCube TUNA mode, where the tip was retracted between each pixel after remaining in contact for 300 ms with a constant deflection trigger of 40 nm to apply the bias voltage. Each sample was measured twice, in different zones, and *I-V* curves at the top of four different NWs for each measurement were collected. Additionally, due to the force applied during TUNA measurement (approximately 1200 nN), the piezotronic effect may be considered. However, the same tip deflection is used for all measurements, and by extension the same applied force on the NW. Therefore, a comparison can be done between the different samples without taking into account the piezotronic effect.

Structural and surface property characterization. Cross-sectional and top-view images of the ZnO NWs were done with a Gemini 300 Field Emission Zeiss SEM. Raman spectroscopy measurements were achieved at room temperature, with an excitation Ar+ laser at 514.5 nm with a 100X lens, using a Jobin Yvon / Horiba Labram spectrometer equipped with a liquid nitrogen cooled CCD detector. X-ray photoelectron spectra were recorded on a ThermoScientific K-Alpha spectrometer using a monochromatized Al Kα radiation source (1486.6 eV), in ultrahigh vacuum (10^{-8} mbar) at room temperature. The X-ray beam area (spot size) was adjusted to 400 µm in diameter. The XPS spectra were acquired in the constant analyzer energy mode using a pass energy of 30 eV and a step size of 0.1 eV for core levels, and a 100 eV pass energy was used for the general survey spectrum (step 0.5 eV). The XPS spectra shown in the figures were averaged over 3 scans for the survey and 10 scans for the core levels. The flood gun was used to neutralize charge effects on the surface.

Optical property measurements. CL measurements were achieved on an FEI Inspect F50 FESEM instrument, using an electron beam with an acceleration voltage of 5 kV and a current of 22 pA. The surface was scanned with a 240 000X magnification (1.25 x 1.25 μm^2 area). The system was cooled down at 5 K with liquid helium. The signal was collected through a parabolic mirror and analyzed with a Horiba iHR550 monochromator, before being recorded with an Andor Technology Newton DU940 BU2 CCD detector. Time-resolved CL measurements were performed at room temperature, using an electron beam with an acceleration voltage of 4 kV and a current of 228 pA, as well as a Hanbury Brown and Twiss interferometer equipped with two fast photomultiplier tubes (PMA Hybrid 06 from PicoQuant). The scanned surface area was of 2.5 x 2.5 μm^2.

Piezoelectric property measurements. PFM measurements were conducted using the same Bruker Dimension Icon AFM as for TUNA measurements. The same PtSi-NCH tips from Bruker were used, and the heavily p-type doped Si (100) substrates also served as the bottom electrodes. The tip calibration was achieved with a PPLN sample for the piezoelectric amplitude ($d_{33} \approx 7.5$ pm/V according to Bruker), and with O- and Zn-polar ZnO single crystals for the phase. Working with rough surfaces, such as vertically aligned ZnO NWs, presented challenges like potential scratching and bending of the NWs. Such issues could lead to contact failure between the tip and the sample. To mitigate these challenges, the DataCube PFM mode was used. This mode involved retracting the tip between each pixel of the image. When the tip made contact with the sample, it remained in contact for 80 ms while applying an AC voltage of 5 V between the tip of the NW and the substrate. This allowed us to collect the resulting piezoelectric deformation of the sample. The presented results for each pixel represent the mean value of the collected signals during this time period. PFM amplitude and phase refer to the tip's oscillation amplitude at the frequency of the PFM modulation and the phase shift between the tip's mechanical oscillations and the PFM modulation voltage, respectively. The PFM modulation frequency was set within the range of 10–15 kHz and ensured that the piezoresponse amplitude and phase remained independent of frequency. This step was performed to prevent any unwanted magnification of the piezoresponse amplitude (parasitic effects).[15,32,33] Additionally, the substantial stiffness of the tip prevented cantilever buckling and significantly reduced electrostatic interferences with the piezoresponse.[34] Each sample was measured twice, in different zones. The amplitude of the piezoelectric response was deduced by filtering the data, such that only the values inside a small square centered at the top surface of the ZnO NW, with a 20 nm^2 area corresponding to the size of the tip, were kept to calculate its mean value. The error bars correspond to the standard deviation of these measurements. This procedure was applied to three different NWs for each sample.

FEM simulation. Finite element method (FEM) simulation was performed using COMSOL Multiphysics software. The geometry of the model used is shown in ***Erreur ! Source du renvoi introuvable.****1* of Supporting Information, along with its dimensions and material considered. The 2D axisymmetric geometry was used as a way to decrease computation time and save computing memory. The thickness of the nucleating layer underneath the NW was set to 50 nm. In ***Erreur ! Source du renvoi introuvable.****1* of Supporting Information are presented the electrical and mechanical boundary conditions, used to consider the semiconductor properties of the NW, related to the free charge carriers and surface traps. The equations used in the model related to the piezoelectric and semiconducting properties of the NWs are the following:

$$[\sigma] = [c][\varepsilon] - [e]^T[E] \tag{1}$$

$$[D] = [e][\varepsilon] + [\kappa][E] \tag{2}$$

with $[\sigma]$ the stress matrix, $[c]$ the elasticity matrix, $[\varepsilon]$ the strain matrix, $[e]$ the piezoelectric coefficient matrix, $[E]$ the electric field vector, $[D]$ the electric displacement vector and $[\kappa]$ the dielectric constant matrix. The coupling between piezoelectric and semiconductor properties is introduced by the two matrices $[e]$ and $[e]^T$, representing the direct and inverse piezoelectric effects, respectively. The local density of charges in Poisson’s equation incorporates the local free carrier densities and average doping concentrations:

$$\nabla \cdot \mathrm{D} = q(\mathrm{p} - \mathrm{n} + N_d - N_a) \tag{3}$$

where n, p are the densities of free electrons and holes and N_d, N_a are the densities of donor and acceptor atoms, respectively. The densities of free electrons and holes depend on both the local electric potential and the ZnO material’s band structures. Additionally, a uniform trap density N_{tt} at the ZnO surface was introduced (see ***Erreur ! Source du renvoi introuvable.****1* of Supporting Information), resulting in a surface charge density expressed as:

$$Q_s = -e^2 N_{tt}(V_s - \varphi_{tf}) \tag{4}$$

where V_s denotes the surface potential, and φ_{tf} represents the difference between the Fermi and intrinsic levels.[31]

3. Results and Discussion

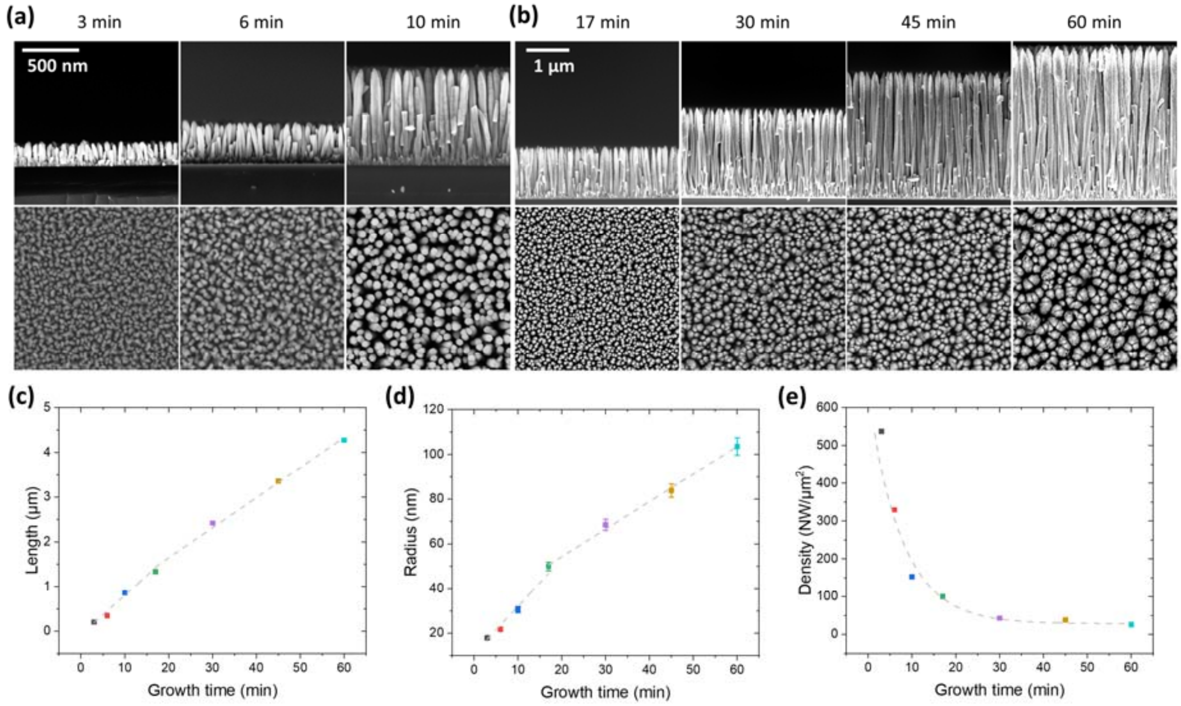

Figure 1. Cross-sectional view and top-view FESEM images of ZnO NWs grown by PLI-MOCVD for different growth times: (a) 3, 6, 10 minutes (b) 17, 30, 45 and 60 minutes (c) Plots of the mean length, (d) mean radius and (e) number density of ZnO NWs as a function of growth time. The evolutions of the mean length and mean radius were fitted with two linear functions for each curve, whereas the evolution of the number density was fitted with a decreasing exponential function. The different fits are represented as the different dashed lines.

3.1. Structural morphology of ZnO nanowires

The structural morphology of ZnO NWs grown by PLI-MOCVD, and the influence of the growth time on their dimensions, are presented in *Figure 1a-b* through cross-sectional view and top-view FESEM images. High resolution transmission electron microscope images of similar structures can be found in Ref 15. The pencil-shaped morphology of these ZnO NWs was observed to differ from the usually flat morphology of ZnO NWs grown with other chemical methods such as chemical bath deposition.[35] As the growth time is increased from 3 to 60 minutes, the mean length and mean radius of ZnO NWs increases from 204 nm to 4.2 µm and from 18 nm to 103 nm, respectively, as depicted in *Figure 1c-d*. The mean length of ZnO NWs linearly increases with the growth time, corresponding to an axial growth rate of 87.28 nm/min from 3 to 17 minutes, and 67.32 nm/min from 17 to 60 minutes. In contrast, their mean radius increases with a radial growth rate of 2.11 nm/min from 3 to 17 minutes, and 1.23 nm/min from 17 to 60 minutes. The decrease in the axial growth rate as the growth time is increased can be explained by the elongating process of ZnO NWs, including the direct impingement of Zn and O gaseous species on its top faces and sidewalls along with the surface diffusion of Zn adsorbed species on the sidewalls.[36,37] As the growth time, and by extension the length, are increased, the Zn adsorbed species at the base of ZnO NWs are no longer able to reach the top faces of ZnO NWs owing to their limited diffusion length and hence the axial growth rate decreases. Here, the transition between the two linear regimes at 17 minutes for both the axial and radial growth rates allows for roughly determining a diffusion length of Zn adsorbed species of about 1.33 µm. *Figure S2* of Supporting Information respectively show the aspect ratio and effective volume of these NWs as a function of growth time. It also reveals two separate growth trends between ZnO NWs grown for 3 to 10 minutes and for 17 to 60 minutes. Accordingly, the number density of these ZnO NWs decreases from 433 to 25 NW/µm^2 as the growth time is increased, as shown in *Figure 1e*. The exponential decrease in the number density is explained by the fact that, while the ZnO NWs radially expand, they occupy more space and undergo a coalescence process into clusters, as observed in top-view FESEM images of *Figure 1a-b*.

3.2. Electrical properties of ZnO nanowires

The repercussion of the surrounding atmosphere on the electrical conduction of ZnO NWs is a critical challenge when proceeding with electrical measurements. Indeed, oxygen molecules from ambient air adsorb on the surface of the ZnO NW, which induce an electron transfer from the NW to the oxygen molecules and therefore reduces its electrical conduction. As a way to control the surrounding atmosphere around the ZnO NW, the electrical measurements were performed *in situ* in a SEM as reported in Ref 38. This method allowed the exposure of the NW with the electron beam in order to remove the species adsorbed on the surfaces and improve its electrical conduction.

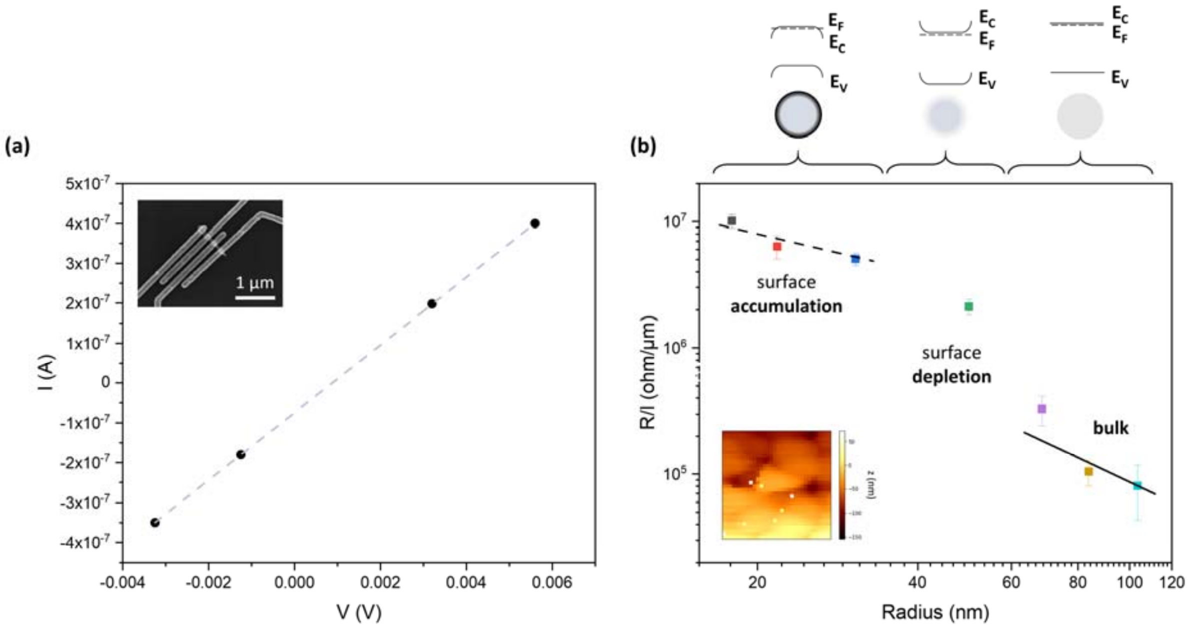

Figure 2. (a) Four-point probe I-V measurement, after an electron beam dose of 4 x 10^5 µC/cm^2, collected on a single contacted ZnO NW grown by PLI-MOCVD with a growth time of 17 minutes, as seen in the inset. (b) Dependence of the R/l ratio (R and l are the resistance and length of the NW, respectively) measured by TUNA with the radius of the NW, with in inset a topography image example of the TUNA measurement on ZnO NWs with a growth time of 17 minutes. The schematic of the energy band diagrams depicted at the top show the different corresponding electrical conduction regimes, according to Ref. 39, where the Fermi level E_F is located close to the conduction band minimum.

A four-point probe *I-V* measurement of a single contacted ZnO NW grown by PLI-MOCVD with a growth time of 17 min, with a 1 µm length and a 50 nm radius, is presented in *Figure 2a*, showing the resulting ohmic behavior. The *I-V* measurement was achieved after an electron beam dose of approximately 4 x 10^5 µC/cm^2. The resistance of the ZnO NW between the two inner contacts was estimated, from the slope of the *I-V* curve, to be of approximately 11.8 kΩ. The present value is consistent with the findings from Bugallo *et al.* reported on a contacted ZnO NW with similar dimensions grown by standard MOCVD, using the same electron beam dose.[39] From the resistance value R, the resistivity ρ was determined from:

$$R = \rho \frac{l}{A} \tag{5}$$

where l is the distance between the inner electrodes (separated of approximately 80 nm) and A is the transverse section area of electrical conduction through the NW related to its radius r. Taking into account the surface charge carrier depletion region thickness d_{spc} due to the oxygen molecule desorption occurring to perform the measurement, the transverse section area is equal to $\pi(r - d_{spc})^2$.[38] The resistivity value is further related directly to the density of charge carriers, in this particular case of free electrons as denoted n, using the following expression:

$$\rho = \frac{1}{q\mu n} \tag{6}$$

with q the electron charge and μ the free electron mobility. The value for the free electron mobility in ZnO NWs has been estimated to be in the range of 50 to 75 $cm^2\ V^{-1}\ s^{-1}$.[40,41] However, in order to estimate n from *Equation 6*, one more unknown needs to be determined, corresponding to the width of the charge carrier depletion region near the surface d_{spc} considered in the transverse section area. Simulation studies from Donatini *et al.* in 2016 evaluated this value at 22 nm, for a NW doping of approximately 10^{18} cm^{-3} and a density of surface traps of 2 x 10^{12} cm^{-2}.[42] However, the dependence of d_{spc} with the doping concentration N_d and the density of surface traps N_t is not given in the literature. In order to coherently estimate n, the value of d_{spc} and its dependence on both concentrations, especially N_d, needs to be determined. To do so, FEM simulations were performed for which the model as well as the method used are shown in *Figures S5-6* of Supplementary Materials. Therefore, the density of free electrons in ZnO NWs grown by PLI-MOCVD is found to lie in the range of 1.8 – 3.3 x 10^{18} cm^{-3}, which is roughly comparable to the range of 1 x 10^{18}–5 x 10^{18} cm^{-3} reported on ZnO NWs grown by standard MOCVD[39,43,44]. Despite the difference from the growth technique itself, for which the PLI-MOCVD system includes the use of a liquid DEZn precursor and solvent as compared to the gaseous ones used in the standard MOCVD system, as well as the lower growth temperature, no significant effects on the free electron density arise. Interestingly, the free electron density in ZnO NWs grown by PLI-MOCVD is thus smaller than the effective critical concentration of 4.2 x 10^{18} cm^{-3} for the Mott transition[45], showing that these ZnO NWs have a nonmetallic electrical conduction.

Though interesting and reliable, the four-point probe technique is not straightforward to be implemented and time-consuming, especially contacting small ZnO NWs with four electrodes. Therefore, to complete this study, Datacube TUNA measurements were performed on all samples. Examples of associated results are shown in Supplementary Materials (see *Figure S3* of Supporting Information). From these *I-V* curves, the resistance of the ZnO NWs was calculated and plotted with respect to their length and as a function of their radius as presented in *Figure 2b*. In 2015, Bugallo *et al.* realized analogous studies by four-point probe I-V measurement and showed the different electrical conduction regimes as a function of the NW radius.[39] With a dependence approximately proportional to $1/r^2$, the electrical conduction is essentially from the bulk. However, a dependence in 1/r corresponds to a surface-like electrical conduction in electron accumulation regime. In *Figure 2b*, the black dotted line agrees with a 1/r fit, and the continuous one to a $1/r^2$. Therefore, we can observe several electrical conduction regimes in this graph, showing its dependence on the radius of the ZnO NW. Below a 30 nm radius, the surface-like electrical conduction in electron accumulation regime is supposed to occur in the ZnO NW, whereas over a 70 nm radius, the electrical conduction essentially originates from the bulk. In the radius range of 30 and 70 nm, another trend is observed, possibly corresponding to a surface-like electrical conduction in electron depletion regime. These statements are supported by the findings from Bugallo *et al.* and Lord *et al.* where they report a dominance from the surface-like electrical conduction in electron accumulation regime below a 20 nm radius and from the surface-like electrical conduction in electron depletion regime below 50 nm.[39,46] The slight variation could come from the differences in the chemical growth methods used. The value of the resistivity can be determined for the ZnO NWs in the case of the bulk-like electrical conduction where the transverse section area of electrical conduction is well known and equal to πr^2. Therefore, an approximated value for the density of free electrons *n* can be calculated using

Equation 6. Assuming the same values for the free electron mobility as previously discussed, this density was determined in the range of 2.5–5.9 x 10^{17} cm^{-3}. These values are slightly lower than the one obtained with the four-point probe electrical measurement for the ZnO NW grown by PLI-MOCVD for 17 minutes. However, the influence of the contact resistance in these electrical measurements cannot be neglected. In addition, these experiments were done in ambient air, possibly meaning that the electrical conductivity of the NWs is somehow influenced by the oxygen molecules adsorbed on their surfaces. It is more complicated to determine the density of free electrons in the case of the surface-like electrical conduction, both in electron accumulation and depletion regimes. However, in electron accumulation regime, the amount of remaining surface charge density n_s can be calculated with the following equation:[39]

$$\frac{R}{l} = \frac{1}{n_s e \mu 2 \pi r} \tag{7}$$

Considering the same values of free electron mobility previously seen, the value of n_s for this particular case lies in the range of 7.8 x 10^{10} to 1.3 x 10^{11} cm^{-2}. These values are slightly lower than the expected amount of surface traps for ZnO NWs grown by vapor phase deposition methods usually found around 10^{12} cm^{-2}.[42,44,46,47] This likely confirms the partial filling of these traps and, consequently, the desorption of oxygen molecules from the surfaces of ZnO NWs.

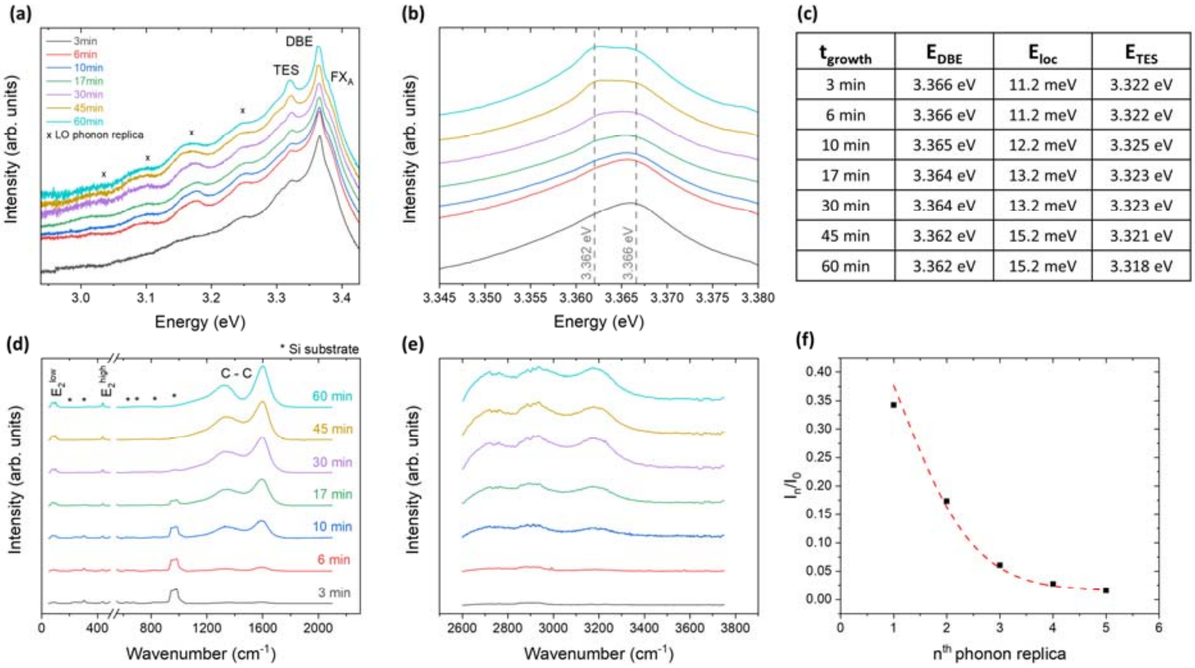

t_{growth}	E_{DBE}	E_{loc}	E_{TES}
3 min	3.366 eV	11.2 meV	3.322 eV
6 min	3.366 eV	11.2 meV	3.322 eV
10 min	3.365 eV	12.2 meV	3.325 eV
17 min	3.364 eV	13.2 meV	3.323 eV
30 min	3.364 eV	13.2 meV	3.323 eV
45 min	3.362 eV	15.2 meV	3.321 eV
60 min	3.362 eV	15.2 meV	3.318 eV

Figure 3. (a) 5K CL spectra in continuous mode of ZnO NWs grown by PLI-MOCVD for different growth times with a cumulative offset and a logarithmic intensity axis (b) Zoom on CL spectra for the DBE peak between 3.345 and 3.380 eV (c) Table of DBE, localization and TES energy values as a function of growth time (d) Raman spectra collected in the ranges of 50 to 2100 cm^{-1} and (e) of 2600 to 3750 cm^{-1} of ZnO NWs grown by PLI-MOCVD for different growth times and with a constant offset (f) Ratios of LO phonon replica to TES line intensities on ZnO NWs grown by PLI-MOCVD for 10 minutes.

3.3. Optical properties of ZnO nanowires

The optical properties of the NWs were evaluated by CL spectroscopy, allowing us to study the nature of their various defects, and supported by Raman spectroscopy. The 5 K CL spectra of ZnO NWs grown by PLI-MOCVD in *Figure 3a* demonstrate that for growth times between 3 to 60 minutes, the near-band-edge (NBE) emission within the 3.0 to 3.5 eV energy range retains its characteristic shape. This emission is dominated by radiative transitions of donor-bound excitons (DBE) located at approximately 3.362–3.366 eV, along with radiative transitions of free A-excitons at about 3.378 eV. The DBE transition around 3.366 eV could be attributed to an excited state of the I_6 line.[48] However, as the growth time of ZnO NWs increases, *Figure 3b* and *c* reveal a shift to lower energies due to an additional contribution around 3.362 eV. This transition could be attributed to the I_6 line, associated with the substitution of Al atoms for Zn sites (Al_{Zn}), possibly due to a residual contamination of the MOCVD system. This supposition could be further supported by the increase of the localization energy E_{loc} from 11.2 to 15.2 meV as the growth time increases, as seen in *Figure 3c*, comparable to the expected one of 15.1 meV for the I_6 line.[49] Alternatively, it may arise from the Z_3 and Z_4 lines, which are associated with the incorporation of carbon species.[50] This assignment is well correlated with the Raman spectra depicted in *Figure 3d*, which exhibits an increase in the carbon concentration in ZnO NWs grown for longer growth times. The estimation of the intensity ratio between both the C-C and E_2^{high} lines confirms the increasing amount of carbon in the NWs as the growth time is increased from 3 to 17 minutes, before reaching a plateau (see *Figure S4* of Supporting Information). This is due to the decomposition of the DEZn chemical precursor used during the growth. Notably, *Figure 3e* does not exhibit any evidence of defects related to hydrogen, thereby confirming their absence when compared to ZnO NWs grown by chemical bath deposition.[51] The hydrogen-based residual species are expected to be evacuated as by-products in the PLI-MOCVD system. Additionally, the second intense line of the NBE emission, located around 3.323 eV in *Figure 3a*, is attributed to radiative transitions involving two-electron satellites (TES) of the I_6 line and hence involving Al_{Zn}. However, the table in *Figure 3c* shows the shift of the peak to lower energies as the growth time is increased from 3 to 60 minutes, demonstrating the addition of a contribution around 3.318 eV possibly due to the progressive formation of basal-plane I_1 stacking faults (BSFs).[15,52,53]

Positioned approximately at 3.251, 3.179, 3.107 and 3.035 eV are the LO phonon replicas of the TES line. Those peaks are separated by an energy of 72 meV, corresponding to the phonon energy in ZnO. These replica exhibit an intensity distribution following a Poisson distribution, as characterized by the following equation:[54]

$$I_n = \frac{e^{-S}.{S_{HR}}^{n}}{n!} I_0 \tag{8}$$

in which n represents the number of the phonon replica, I_n is the intensity of the n^{th} replica, I_0 is the intensity of the TES line, and S_{HR} represents the Huang-Rhys constant. This constant reflects the coupling strength between electronic transitions and the LO polarization field. In *Figure 3f*, a Poisson fit example illustrates the determination of the S_{HR} value, displaying I_n over I_0 as a function of the n^{th} phonon replica in ZnO NWs grown for 10 minutes. In this case, the calculated value of S_{HR} hovers around 0.8, which is consistent with the expectations for ZnO NWs grown by PLI-MOCVD.[15] This somehow rules out the role of the TES line involving Al_{Zn} for which the S value of 0.058 was reported,[54] at the benefit of the major contribution of the BSF line on which the localization may be enhanced. The S_{HR} values in ZnO NWs grown for other growth times appear slightly lower, ranging between 0.1 and 0.5.

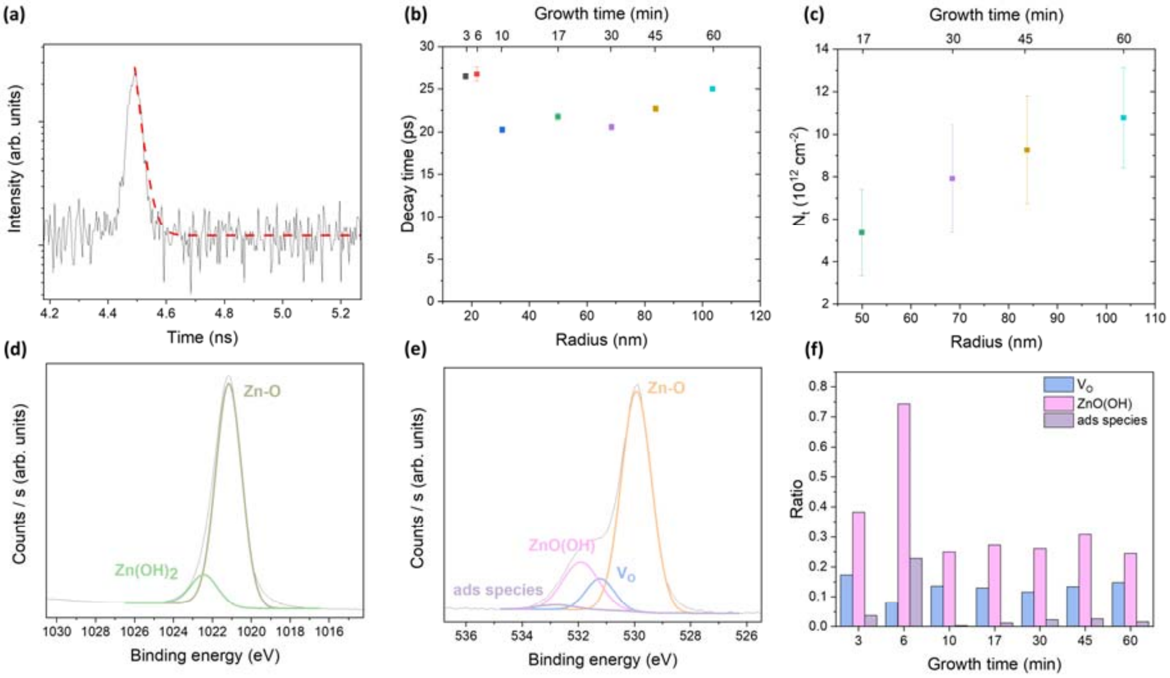

Figure 4. (a) Plot of the CL intensity decrease in ZnO NWs grown by PLI-MOCVD for 10 minutes with a decreasing exponential fit as the red dashed line (b) Resulting decay time plotted as a function of NW radius and growth time (c) Surface trap density N_t as a function of NW radius and growth time (d) XPS spectrum of ZnO NWs grown by PLI-MOCVD for 10 minutes corresponding to the Zn2p core levels and its fitting (e) XPS spectrum of ZnO NWs grown by PLI-MOCVD for 10 minutes corresponding to the O1s core levels and its fitting (f) Fitted curve area ratio of O1s contributions over Zn-O contributions.

The Raman spectra depicted in *Figure 3d* indicate the improvement of the crystallinity of ZnO NWs as the growth time is increased from 3 to 60 minutes, owing to the increase in the intensity of both E_2^{low} and E_2^{high} lines pointing at 99 and 438 cm^{-1}, respectively.[55]

Furthermore, the surface properties of ZnO NWs were investigated by time-resolved CL measurements, and supported by XPS. An example of the resulting CL intensity exponential decay recorded during these measurements is presented in *Figure 4a* in the case of ZnO NWs grown by PLI-MOCVD for 10 minutes. The fitting of this curve with an exponential law, as presented with the red dashed line, allowed us to determine the associated decay time. The determination of this value can lead to the estimation of the surface recombination velocity S, which is related to the density of traps on the surfaces of the ZnO NWs N_t by the relation $S = \sigma v_{th} N_t$, where σ is the capture cross section of the recombination center and v_{th} is the thermal hole velocity. The relation between τ^*, as the effective lifetime, and S is described by the following equation:[42]

$$\frac{1}{\tau^*} = \frac{1}{\tau_B} + \frac{2S}{r - d_{spc}} \tag{9}$$

where τ_B is the exciton bulk lifetime with a value of 10 ns for ZnO,[56] r is the radius of the NW and d_{spc} is the width of the charge carrier depletion region near the surface that results from the Fermi level pinning effect occurring at the surface of the NW.[57] *Figure 4b* illustrates the relationship between the decay time and the radius of the NWs. As the NW radius increases, the decay time exhibits several variations. Initially, for small NWs with a radius of approximately 20 nm, the decay time lies between 25 and 26 ps. However, as the radius increases to 30 nm, the decay time decreases to around 20 ps, but it increases again up to approximately 25 ps as the NW radius continues to grow. A conclusion on the impact of the radius on the density of surface traps cannot be obtained only based on this trend. Using the same method as for the calculation of n presented in *Figure S5* and *S6* of Supporting Information, the expected values of N_t were determined from *Equation 9*. The results, as a function of growth time and NW radius, are depicted in *Figure 4c*, showing an increase from approximately 5 x 10^{12} to 1 x 10^{13} cm^{-2} as the radius of the NW increases from 50 to 100 nm. Nevertheless, for a radius below a certain value, the NW becomes completely depleted (see *Figure S7*), making this solving method unsuitable. To compare these values with literature, the values expected for NWs grown by vapor phase deposition methods, are around 10^{12} cm^{-2}.[42,44,46,47] The order of magnitude obtained confirms the validity of the solving method. The small difference could be explained by the fact that the PLI-MOCVD system used in this case is different than the one from the literature due to the deposition at lower temperature and with the zinc precursor in liquid form. In 2012, Soudi *et al.* studied the dependence of N_t with the NW radius, showing the decrease in the density of surface states as the radius increases.[47] However, the radius of the NWs studied in this report lay between 30 to 60 nm, a range where the density of surface traps could not be estimated in our case. Therefore, a different trend could be expected for small and wider NWs.

To support these results on the surface properties, XPS measurements of ZnO NWs grown by PLI-MOCVD for different growth times were performed. Examples of these XPS measurements in ZnO NWs grown for 10 minutes, and the fitted curve area ratio of their different contributions, are presented in *Figure 4d-f*. *Figure 4d* represents the detection of zinc related peaks, in this case Zn-O and $Zn(OH)_2$ bonds. The detection of oxygen related bonds are represented in *Figure 4e*, with Zn-O, the oxygen vacancies, ZnO(OH) and adsorbed species such as C-O, C=O or H_2O, respectively at 529.9 eV, 531.2 eV, 531.9 eV and 533 eV.[58] *Figure 4f* shows the fitted curve area ratio with Zn-O of the oxygen vacancies (V_O), ZnO(OH) and adsorbed species contributions. The evolution of these ratios as a function of growth time demonstrates a difference between the ZnO NWs with a radius around 20 nm, where the ratio of ZnO(OH) defects is especially higher, and the ZnO NWs with a wider radius. This observation can be compared with *Figure 4b*, showing a similar discrepancy between small NWs with a radius around 20 nm and wider ones. Therefore, this could confirm the possible reverse trend expected, demonstrating a larger amount of surface traps in smaller NWs.[47]

3.4. Piezoelectric properties of ZnO nanowires

The amplitude and phase of the piezoelectric response as measured by DataCube PFM on the ZnO NWs grown by PLI-MOCVD for different growth times are presented in *Figure 5a-b*. The amplitude of the piezoelectric response for the ZnO NWs with the different dimensions, as shown in *Figure 5a*, lies in the range of 0–35 pm, by applying a 5 V AC voltage between the substrate and the AFM tip (grounded). The phase of the piezoelectric response, as depicted in *Figure 5b*, shows a great homogeneity on the positive side (light areas) with a value around 70°, corresponding to the Zn-polarity on the top surface of the ZnO NWs. *Figure 5c* shows the d_{33}^{eff} piezoelectric coefficient as a function of NW radius. This coefficient depends on the piezoelectric amplitude and can therefore be calculated with the following formula:

$$d_{33}^{eff} = \frac{Amplitude}{Applied\ Voltage} \qquad (10)$$

where the amplitude considered here is the one filtered as mentioned in the experimental procedure

and the applied voltage is equal to 5 V in this particular case. The values of d_{33}^{eff} were found to lie in the range of 4.5 to 5.5 pm/V. As observed in *Figure 5c*, the variation of d_{33}^{eff} as a function of NW radius does not show any particular trend. In comparison, FEM simulations have suggested the impact of the radius to be significant, more specifically, smaller radii showed an improved piezoelectric response.[31] However, the present FEM simulations were achieved for a vertically integrated nanogenerator (VING) model, making the comparison with PFM measurements irrelevant. Moreover, in these FEM simulations, the length of ZnO NWs was considered to retain a constant value, which is not the case here.

In order to more accurately compare these PFM measurements with theoretical calculations, FEM simulations were carried out using COMSOL Multiphysics software. In agreement with previous studies,[27,31,32] static simulations were conducted, as the PFM amplitude remains unaffected by the PFM modulation frequency. The geometry considered in this study is depicted in *Figure 5d*. The thickness of the ZnO nucleating layer was set to 50 nm. The mean length and radius of ZnO NWs deduced from the FESEM images were used in the model as input parameters. The platinum (Pt) 20 nm^2 surface square on the top of the NW represents the conductive tip used in PFM measurements. Mechanical and electrical boundary conditions, as well as the equations related to the piezoelectric and semiconducting properties of the material, are discussed in Paragraph 2. However, in this case, an applied voltage on the top of the conductive tip was added. The values of the density of free charges *n* obtained in paragraph 3.2, 1.8 x 10^{18} and 3.3 x 10^{18} cm^{-3}, were used in the model, with the assumption that the density of doping charges N_d is equal to *n*. For the density of surface traps N_t, the values from 4 x 10^{12} cm^{-2} to 1 x 10^{13} cm^{-2} determined previously were used for ZnO NWs grown for 17 to 60 minutes. For smaller NWs, the interval of values between 10^{12} cm^{-2} to 10^{13} cm^{-2} was considered. This choice is coherent with the small variation in the results, even with an order of magnitude of difference in the density of surface traps. Indeed, at such small dimensions, the NW is completely or almost completely depleted, the density of surface traps having a low impact on the piezoelectric response. To simplify the model, we assumed the traps were slow, resulting in a charge that remained fixed as the applied voltage varied.[30] Consequently, the boundary condition at the interfaces of ZnO NWs was based on the local surface voltage obtained in the initial state, making the surface charge dependent upon their position but not upon the time. The amplitude of the piezoelectric response was calculated as the displacement of the top surface resulting from a change in the applied potential to the tip, starting from an initial value $V_i = 0$ and ending at a final value $V_f = -1$ as in Ref 27.

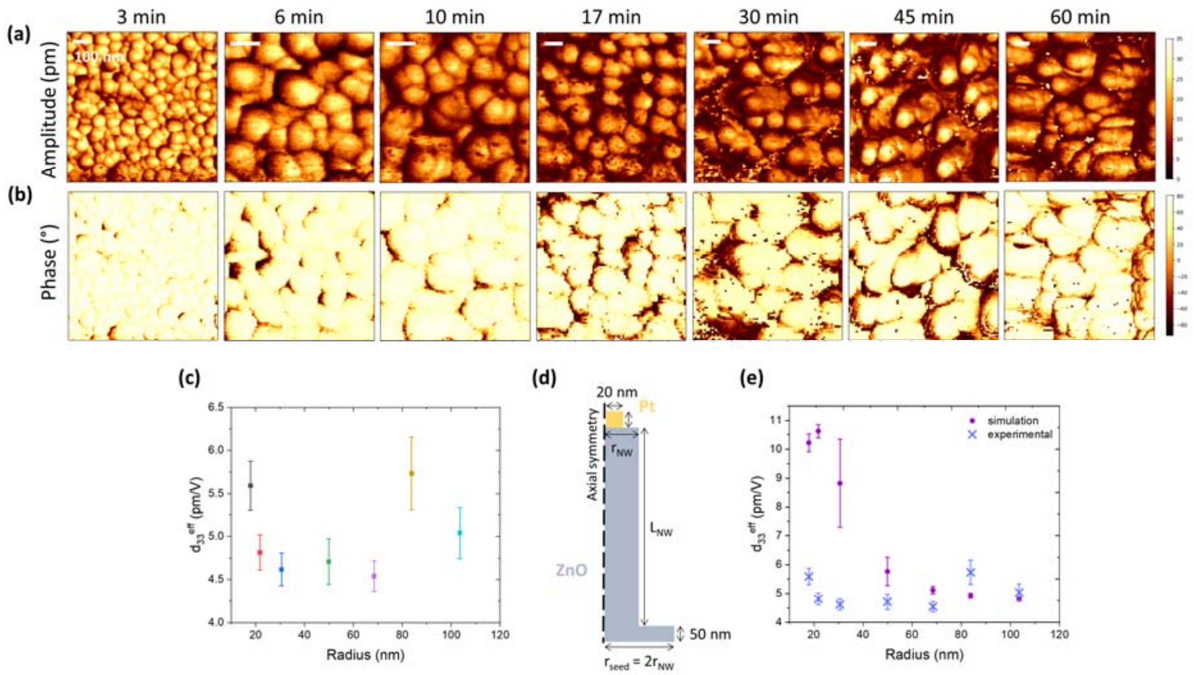

Figure 5. PFM measurements showing (a) the amplitude of the piezoelectric response and (b) the piezoelectric phase of ZnO NWs grown by PLI-MOCVD for different growth times (c) d_{33}^{eff} *coefficient from PFM measurement as a function of the NWs radius (d) Geometry, dimensions and materials of the FEM model (e)* d_{33}^{eff} *coefficient from simulation, compared with experimental results, as a function of NW radius*

Figure 5e shows the results obtained in FEM simulation, compared with experimental results discussed previously, plotting the d_{33}^{eff} coefficient as a function of the NW radius. The error bars for simulation results are due to the uncertainty in the values of n and N_t from experimental results. Coherence is found between theoretical and experimental results for NWs with a radius over 50 nm, confirming the validity of the previous results on the density of both donor and surface charges. However, discrepancy in the results is found for smaller NWs. This could be explained by the fact that, at these dimensions, the radius of the tip is in the same order of magnitude as the radius of the wires. Therefore, difficulties could occur during the PFM measurements, decreasing the piezoelectric response. Indeed, the measurement could be impacted by the NWs near neighbors. However, in paragraph 3.1, *Figure 1e* showed the exponential decrease of the density as a function of the growth time. The effect of the density could be critical and explain the divergence between experimental and theoretical work for smaller NWs.

3.5. Discussion

The dimension tuning of ZnO NWs demonstrates a variation on their properties as the growth time is increased. Above 17 min growth, the axial growth rate decreases due to the limited diffusion length of the different species (approximated around 1.33 µm). The Zn and O species adsorbed and diffused from the substrate and sidewalls of ZnO NWs can no longer reach the growing top face, explaining this decreasing growth rate. This phenomenon correlates to the incorporation of carbon related defects as observed in *Figure S4* of Supporting Information, obtained from Raman spectroscopy measurements, where we first observe an increase of the carbon content as a function of growth time from 3 to 17 minutes. Above 17 min growth time, we observe a saturation of the carbon-related defect incorporation. Therefore, the density of free electrons in the range of 1.8 to 3.3 x 10^{18} cm^{-3}, determined from four-point probe resistivity measurement and related to the concentration of shallow donors, possibly stays in a similar range for ZnO NWs grown from 17 to 60 min. However, this density is possibly lower for ZnO NWs grown from 3 to 10 min, due to the lower concentration of carbon-related defects. To confirm this assumption, TUNA measurements have shown a surface like electrical conduction in accumulation for those same ZnO NWs suggesting the presence of either a low density of free electrons, where the electrical conduction is so minimal that most electrons are concentrated at the surface, or a high density of surface traps, which may attract and capture most of the free electrons.[39] For ZnO NWs grown for 3 and 6 minutes, CL time resolved measurement have shown an increase in the exciton effective lifetime compared to ZnO NWs grown for higher growth times. The computation of the surface trap density could not be achieved for such NWs, however, this exciton lifetime increase could support the hypothesis of a surface trap density higher than 1 x 10^{13} cm^{-2}. Unfortunately, these two suppositions are insufficient to account for the small discrepancy between experimental and theoretical computations of the piezoelectric coefficient at these smaller radii. Owing to their small size and high density, the impact of neighboring ZnO NWs on the piezoelectric response of one single NW during PFM measurements is not negligible and likely has a high influence on the resulting piezoelectric response amplitude.

4. Conclusion

In summary, the different contributions to the piezoelectric response of ZnO NWs, originating from the dimensionality effect, the nature of defects, the density of free charge carriers, as well as the nature and density of surface traps, has theoretically and experimentally been decoupled. The tuning of the dimensions of ZnO NWs in terms of radius and length has been achieved using PLI-MOCVD, allowing us to thoroughly investigate their structural, electrical, optical, surface, and piezoelectric properties as well as their dependence on the size. As the growth time is increased, separate growth trends have been observed, related to the limited diffusion length of Zn adsorbed species estimated around 1.33 µm. The density of free electrons has been determined using four-point probe resistivity measurements in a SEM equipment and found to lie in the range of 1.8 – 3.3 x 10^{18} cm^{-3} for ZnO NWs with a 50 nm radius. Additional TUNA measurements in an AFM equipment have provided a deep analysis of the electrical conductivity behavior of the ZnO NWs as a function of their radius, showing a transition between the surface and bulk electrical conduction below a 70 nm radius. Continuous CL spectroscopy coupled with Raman spectroscopy have been achieved to determine the nature and amount of defects in the bulk of ZnO NWs, showing the introduction of Al_{Zn} and carbon species as well as the formation of stacking faults at longer growth times, in addition to the absence of hydrogen-related defects. Furthermore, time-resolved CL spectroscopy combined with FEM simulations have given an estimation of the density of surface traps ranging from 5 x 10^{12} to 1 x 10^{13} cm^{-2} as the radius of ZnO NWs is increased above 50 nm. PFM measurements and their dependence on the radius and length of ZnO NWs have been performed to determine their piezoelectric properties. Those results have shown that ZnO NWs are uniformly of Zn-polarity and exhibit a piezoelectric coefficient in the range of 4.5 to 5.5 pm/V. Their comparison with FEM simulation have allowed us to gain a deeper understanding on how the piezoelectric response of ZnO NWs is dependent upon the density of free electrons and the density of surface traps, both of them being intricate and influenced by their dimensions. These findings open valuable perspectives towards the fabrication of more efficient mechanical energy transducers made of ZnO NWs.

Supporting Information

COMSOL model with geometry, dimensions and material electrical and mechanical boundary conditions (*Figure S1*); Aspect ratio and volume of ZnO NWs grown by PLI-MOCVD as a function of growth time (*Figure S2*); Datacube TUNA topography images and their related I-V curves at 4 points chosen near the top of ZnO NWs (*Figure S3*); Intensity ratio of the C-C and E_2^{low} lines over the E_2^{high} line (*Figure S4*); Space charge density as a function of N_{tt} and N_d (*Figure S5*); Surface depletion region thickness d_{sur} as a function of N_{tt} and N_d as well as n obtained by computation as a function of N_d value supposed in the FEM simulation (*Figure S6*); Space charge density map as a function of NW radius (*Figure S7*).

Acknowledgments

This work was supported by the French National Research Agency through the project SCENIC (ANR-20-CE09-0005). L.L. held a doctoral fellowship from the project SCENIC. The authors further acknowledge the support by the French RENATECH network through the PTA technological platforms in Grenoble. This research has also benefited from some of the characterization equipments of the Grenoble INP-CMTC platform and from the facilities and expertise of the OPE)N(RA characterization platform of FMNT (FR 2542, fmnt.fr) supported by CNRS, Grenoble INP and UGA.

References

(1) Wang, Z. L.; Song, J. Piezoelectric Nanogenerators Based on Zinc Oxide Nanowire Arrays. *Science* **2006**, *312* (5771), 242–246. https://doi.org/10.1126/science.1124005.

(2) Zhu, G.; Yang, R.; Wang, S.; Wang, Z. L. Flexible High-Output Nanogenerator Based on Lateral ZnO Nanowire Array. *Nano Lett.* **2010**, *10* (8), 3151–3155. https://doi.org/10.1021/nl101973h.

(3) Xu, S.; Qin, Y.; Xu, C.; Wei, Y.; Yang, R.; Wang, Z. L. Self-Powered Nanowire Devices. *Nat. Nanotechnol.* **2010**, *5* (5), 366–373. https://doi.org/10.1038/nnano.2010.46.

(4) Yu, A.; Li, H.; Tang, H.; Liu, T.; Jiang, P.; Wang, Z. L. Vertically Integrated Nanogenerator Based on ZnO Nanowire Arrays. *Phys. Status Solidi RRL – Rapid Res. Lett.* **2011**, *5* (4), 162–164. https://doi.org/10.1002/pssr.201105120.

(5) Wang, Z.; Pan, X.; He, Y.; Hu, Y.; Gu, H.; Wang, Y. Piezoelectric Nanowires in Energy Harvesting Applications. *Adv. Mater. Sci. Eng.* **2015**, *2015*, e165631. https://doi.org/10.1155/2015/165631.

(6) Wang, X.; Zhou, J.; Song, J.; Liu, J.; Xu, N.; Wang, Z. L. Piezoelectric Field Effect Transistor and Nanoforce Sensor Based on a Single ZnO Nanowire. *Nano Lett.* **2006**, *6* (12), 2768–2772. https://doi.org/10.1021/nl061802g.

(7) Wu, W.; Wen, X.; Wang, Z. L. Taxel-Addressable Matrix of Vertical-Nanowire Piezotronic Transistors for Active and Adaptive Tactile Imaging. *Science* **2013**, *340* (6135), 952–957. https://doi.org/10.1126/science.1234855.

(8) Han, W.; Zhou, Y.; Zhang, Y.; Chen, C.-Y.; Lin, L.; Wang, X.; Wang, S.; Wang, Z. L. Strain-Gated Piezotronic Transistors Based on Vertical Zinc Oxide Nanowires. *ACS Nano* **2012**, *6* (5), 3760–3766. https://doi.org/10.1021/nn301277m.

(9) He, J. H.; Hsin, C. L.; Liu, J.; Chen, L. J.; Wang, Z. L. Piezoelectric Gated Diode of a Single ZnO Nanowire. *Adv. Mater.* **2007**, *19* (6), 781–784. https://doi.org/10.1002/adma.200601908.

(10) Tao, R.; Parmar, M.; Ardila, G.; Oliveira, P.; Marques, D.; Montès, L.; Mouis, M. Performance of ZnO Based Piezo-Generators under Controlled Compression. *Semicond. Sci. Technol.* **2017**, *32* (6), 064003. https://doi.org/10.1088/1361-6641/aa691f.

(11) Villafuerte, J.; Zhang, X.; Sarigiannidou, E.; Donatini, F.; Chaix-Pluchery, O.; Rapenne, L.; Le, M.-Q.; Petit, L.; Pernot, J.; Consonni, V. Boosting the Piezoelectric Coefficients of Flexible Dynamic Strain Sensors Made of Chemically-Deposited ZnO Nanowires Using Compensatory Sb Doping. *Nano Energy* **2023**, *114*, 108599. https://doi.org/10.1016/j.nanoen.2023.108599.

(12) Liu, Y.; Gorla, C. R.; Liang, S.; Emanetoglu, N.; Lu, Y.; Shen, H.; Wraback, M. Ultraviolet Detectors Based on Epitaxial ZnO Films Grown by MOCVD. *J. Electron. Mater.* **2000**, *29* (1), 69–74. https://doi.org/10.1007/s11664-000-0097-1.

(13) Lee, W.; Jeong, M.-C.; Myoung, J.-M. Catalyst-Free Growth of ZnO Nanowires by Metal-Organic Chemical Vapour Deposition (MOCVD) and Thermal Evaporation. *Acta Mater.* **2004**, *52* (13), 3949–3957. https://doi.org/10.1016/j.actamat.2004.05.010.

(14) Park, W. i.; Yi, G.-C.; Kim, M.; Pennycook, S. j. ZnO Nanoneedles Grown Vertically on Si Substrates by Non-Catalytic Vapor-Phase Epitaxy. *Adv. Mater.* **2002**, *14* (24), 1841–1843. https://doi.org/10.1002/adma.200290015.

(15) Bui, Q. C.; Ardila, G.; Sarigiannidou, E.; Roussel, H.; Jiménez, C.; Chaix-Pluchery, O.; Guerfi, Y.; Bassani, F.; Donatini, F.; Mescot, X.; Salem, B.; Consonni, V. Morphology Transition of ZnO from Thin Film to Nanowires on Silicon and Its Correlated Enhanced Zinc Polarity Uniformity and Piezoelectric Responses. *ACS Appl. Mater. Interfaces* **2020**, *12* (26), 29583–29593. https://doi.org/10.1021/acsami.0c04112.

(16) Zhang, B. P.; Wakatsuki, K.; Binh, N. T.; Usami, N.; Segawa, Y. Effects of Growth Temperature on the Characteristics of ZnO Epitaxial Films Deposited by Metalorganic Chemical Vapor Deposition. *Thin Solid Films* **2004**, *449* (1), 12–19. https://doi.org/10.1016/S0040-6090(03)01466-4.

(17) Sallet, V.; Thiandoume, C.; Rommeluere, J. F.; Lusson, A.; Rivière, A.; Rivière, J. P.; Gorochov, O.; Triboulet, R.; Muñoz-Sanjosé, V. Some Aspects of the MOCVD Growth of ZnO on Sapphire Using Tert-Butanol. *Mater. Lett.* **2002**, *53* (1), 126–131. https://doi.org/10.1016/S0167-577X(01)00558-4.

(18) Montenegro, D. N.; Souissi, A.; Martínez-Tomás, C.; Muñoz-Sanjosé, V.; Sallet, V. Morphology Transitions in ZnO Nanorods Grown by MOCVD. *J. Cryst. Growth* **2012**, *359*, 122–128. https://doi.org/10.1016/j.jcrysgro.2012.08.038.

(19) Yao, B. D.; Chan, Y. F.; Wang, N. Formation of ZnO Nanostructures by a Simple Way of Thermal Evaporation. *Appl. Phys. Lett.* **2002**, *81* (4), 757–759. https://doi.org/10.1063/1.1495878.

(20) Qin, W.; Li, T.; Li, Y.; Qiu, J.; Ma, X.; Chen, X.; Hu, X.; Zhang, W. A High Power ZnO Thin Film Piezoelectric Generator. *Appl. Surf. Sci.* **2016**, *364*, 670–675. https://doi.org/10.1016/j.apsusc.2015.12.178.

(21) Tao, R.; Ardila, G.; Parmar, M.; Michaud, L.; Mouis, M. Flexible Piezoelectric Transducers Based on a PMMA/ZnO Nanowire Composite. In *2017 Joint International EUROSOI Workshop and International Conference on Ultimate Integration on Silicon (EUROSOI-ULIS)*; 2017; pp 188–191. https://doi.org/10.1109/ULIS.2017.7962558.

(22) Malandrino, G.; Blandino, M.; Fragala, M. E.; Losurdo, M.; Bruno, G. Relationship between Nanostructure and Optical Properties of ZnO Thin Films. *J. Phys. Chem. C* **2008**, *112* (26), 9595–9599. https://doi.org/10.1021/jp8001492.

(23) Black, K.; Chalker, P. R.; Jones, A. C.; King, P. J.; Roberts, J. L.; Heys, P. N. A New Method for the Growth of Zinc Oxide Nanowires by MOCVD Using Oxygen-Donor Adducts of Dimethylzinc. *Chem. Vap. Depos.* **2010**, *16* (1–3), 106–111. https://doi.org/10.1002/cvde.200906831.

(24) Jeong, M.-C.; Oh, B.-Y.; Lee, W.; Myoung, J.-M. Comparative Study on the Growth Characteristics of ZnO Nanowires and Thin Films by Metalorganic Chemical Vapor Deposition (MOCVD). *J. Cryst. Growth* **2004**, *268* (1), 149–154. https://doi.org/10.1016/j.jcrysgro.2004.05.019.

(25) Sénateur, J.-P.; Dubourdieu, C.; Weiss, F.; Rosina, M.; Abrutis, A. Pulsed Injection MOCVD of Functional Electronic Oxides. *Adv. Mater. Opt. Electron.* **2000**, *10* (3–5), 155–161. https://doi.org/10.1002/1099-0712(200005/10)10:3/5<155::AID-AMO406>3.0.CO;2-2.

(26) Bui, Q. C.; Consonni, V.; Boubenia, S.; Gay, G.; Perret, C.; Zeghouane, M.; Labau, S.; Jiménez, C.; Roussel, H.; Mescot, X.; Ardila, G.; Salem, B. Influence of the AZO Electrode on ZnO Nanowire Growth by PLI-MOCVD and Related Piezoelectric Performance: Implications for Mechanical Energy Transducers. *ACS Appl. Nano Mater.* **2023**, *6* (9), 7436–7445. https://doi.org/10.1021/acsanm.3c00608.

(27) Jalabert, T.; Pusty, M.; Mouis, M.; Ardila, G. Investigation of the Diameter-Dependent Piezoelectric Response of Semiconducting ZnO Nanowires by Piezoresponse Force Microscopy and FEM Simulations. *Nanotechnology* **2023**, *34* (11), 115402. https://doi.org/10.1088/1361-6528/acac35.

(28) Bui, Q. C.; Consonni, V.; Jiménez, C.; Roussel, H.; Mescot, X.; Salem, B.; Ardila, G. Correlation between the Dimensions and Piezoelectric Properties of ZnO Nanowires Grown by PLI-MOCVD with Different Flow Rates. *Nanoenergy Adv.* **2023**, *3* (3), 220–235. https://doi.org/10.3390/nanoenergyadv3030011.

(29) Manrique, M.; Consonni, V.; Boubenia, S.; Roussel, H.; Zeghouane, M.; Labau, S.; Cavalaglio, S.; Pudda, C.; Jacob, V.; Le Rhun, G.; Salem, B. Enhancing the Output Voltage of Piezoelectric Nanogenerators Based on ZnO Nanowires Grown by Chemical Bath Deposition Using Compensatory Cu Doping. *Energy Technol.* **2024**, *12* (5), 2301381. https://doi.org/10.1002/ente.202301381.

(30) Garcia, A. J. L.; Mouis, M.; Cresti, A.; Tao, R.; Ardila, G. Influence of Slow or Fast Surface Traps on the Amplitude and Symmetry of the Piezoelectric Response of Semiconducting-Nanowire-Based Transducers. *J. Phys. Appl. Phys.* **2022**, *55* (40), 405502. https://doi.org/10.1088/1361-6463/ac8251.

(31) Lopez Garcia, A. J.; Mouis, M.; Consonni, V.; Ardila, G. Dimensional Roadmap for Maximizing the Piezoelectrical Response of ZnO Nanowire-Based Transducers: Impact of Growth Method. *Nanomaterials* **2021**, *11* (4), 941. https://doi.org/10.3390/nano11040941.

(32) Garcia, A. J. L.; Jalabert, T.; Pusty, M.; Defoor, V.; Mescot, X.; Montanino, M.; Sico, G.; Loffredo, F.; Villani, F.; Nenna, G.; Ardila, G. Size and Semiconducting Effects on the Piezoelectric Performances of ZnO Nanowires Grown onto Gravure-Printed Seed Layers on Flexible Substrates. *Nanoenergy Adv.* **2022**, *2* (2), 197–209. https://doi.org/10.3390/nanoenergyadv2020008.

(33) Jaloustre, L.; Le Denmat, S.; Auzelle, T.; Azadmand, M.; Geelhaar, L.; Dahlem, F.; Songmuang, R. Toward Quantitative Measurements of Piezoelectricity in III-N Semiconductor Nanowires. *ACS Appl. Nano Mater.* **2021**, *4* (1), 43–52. https://doi.org/10.1021/acsanm.0c02078.

(34) Kim, S.; Seol, D.; Lu, X.; Alexe, M.; Kim, Y. Electrostatic-Free Piezoresponse Force Microscopy. *Sci. Rep.* **2017**, *7* (1), 41657. https://doi.org/10.1038/srep41657.

(35) Parize, R.; Garnier, J.; Chaix-Pluchery, O.; Verrier, C.; Appert, E.; Consonni, V. Effects of Hexamethylenetetramine on the Nucleation and Radial Growth of ZnO Nanowires by Chemical Bath Deposition. *J. Phys. Chem. C* **2016**, *120* (9), 5242–5250. https://doi.org/10.1021/acs.jpcc.6b00479.

(36) Consonni, V.; Dubrovskii, V. G.; Trampert, A.; Geelhaar, L.; Riechert, H. Quantitative Description for the Growth Rate of Self-Induced GaN Nanowires. *Phys. Rev. B* **2012**, *85* (15), 155313. https://doi.org/10.1103/PhysRevB.85.155313.

(37) Kim, D. S.; Gösele, U.; Zacharias, M. Surface-Diffusion Induced Growth of ZnO Nanowires. *J. Cryst. Growth* **2009**, *311* (11), 3216–3219. https://doi.org/10.1016/j.jcrysgro.2009.03.026.

(38) Donatini, F.; Sartel, C.; Sallet, V.; Pernot, J. Electron Beam Dose Dependence of Surface Recombination Velocity and Surface Space Charge in Semiconductor Nanowires. *Nanotechnology* **2017**, *28* (23), 235701. https://doi.org/10.1088/1361-6528/aa70be.

(39) Bugallo, A. D. L.; Donatini, F.; Sartel, C.; Sallet, V.; Pernot, J. Metallic Core Conduction in Unintentionally Doped ZnO Nanowire. *Appl. Phys. Express* **2015**, *8* (2), 025001. https://doi.org/10.7567/APEX.8.025001.

(40) Kälblein, D.; Weitz, R. T.; Böttcher, H. J.; Ante, F.; Zschieschang, U.; Kern, K.; Klauk, H. Top-Gate ZnO Nanowire Transistors and Integrated Circuits with Ultrathin Self-Assembled Monolayer Gate Dielectric. *Nano Lett.* **2011**, *11* (12), 5309–5315. https://doi.org/10.1021/nl202767h.

(41) Park, W. I.; Kim, J. S.; Yi, G.-C.; Bae, M. H.; Lee, H.-J. Fabrication and Electrical Characteristics of High-Performance ZnO Nanorod Field-Effect Transistors. *Appl. Phys. Lett.* **2004**, *85* (21), 5052–5054. https://doi.org/10.1063/1.1821648.

(42) Donatini, F.; de Luna Bugallo, A.; Tchoulfian, P.; Chicot, G.; Sartel, C.; Sallet, V.; Pernot, J. Comparison of Three E-Beam Techniques for Electric Field Imaging and Carrier Diffusion Length Measurement on the Same Nanowires. *Nano Lett.* **2016**, *16* (5), 2938–2944. https://doi.org/10.1021/acs.nanolett.5b04710.

(43) Wang, L.; Chauveau, J. M.; Brenier, R.; Sallet, V.; Jomard, F.; Sartel, C.; Brémond, G. Access to Residual Carrier Concentration in ZnO Nanowires by Calibrated Scanning Spreading Resistance Microscopy. *Appl. Phys. Lett.* **2016**, *108* (13), 132103. https://doi.org/10.1063/1.4945100.

(44) Hertog, M. den; Donatini, F.; McLeod, R.; Monroy, E.; Sartel, C.; Sallet, V.; Pernot, J. In Situ Biasing and Off-Axis Electron Holography of a ZnO Nanowire. *Nanotechnology* **2017**, *29* (2), 025710. https://doi.org/10.1088/1361-6528/aa923c.

(45) Brochen, S.; Feuillet, G.; Santailler, J.-L.; Obrecht, R.; Lafossas, M.; Ferret, P.; Chauveau, J.-M.; Pernot, J. Non-Metal to Metal Transition in n-Type ZnO Single Crystal Materials. *J. Appl. Phys.* **2017**, *121* (9), 095704. https://doi.org/10.1063/1.4977506.

(46) Lord, A. M.; Maffeis, T. G.; Walton, A. S.; Kepaptsoglou, D. M.; Ramasse, Q. M.; Ward, M. B.; Köble, J.; Wilks, S. P. Factors That Determine and Limit the Resistivity of High-Quality Individual ZnO Nanowires. *Nanotechnology* **2013**, *24* (43), 435706. https://doi.org/10.1088/0957-4484/24/43/435706.

(47) Soudi, A.; Hsu, C.-H.; Gu, Y. Diameter-Dependent Surface Photovoltage and Surface State Density in Single Semiconductor Nanowires. *Nano Lett.* **2012**, *12* (10), 5111–5116. https://doi.org/10.1021/nl301863e.

(48) Meyer, B. K.; Sann, J.; Eisermann, S.; Lautenschlaeger, S.; Wagner, M. R.; Kaiser, M.; Callsen, G.; Reparaz, J. S.; Hoffmann, A. Excited State Properties of Donor Bound Excitons in ZnO. *Phys. Rev. B* **2010**, *82* (11), 115207. https://doi.org/10.1103/PhysRevB.82.115207.

(49) Meyer, B. K.; Alves, H.; Hofmann, D. M.; Kriegseis, W.; Forster, D.; Bertram, F.; Christen, J.; Hoffmann, A.; Straßburg, M.; Dworzak, M.; Haboeck, U.; Rodina, A. V. Bound Exciton and Donor–Acceptor Pair Recombinations in ZnO. *Phys. Status Solidi B* **2004**, *241* (2), 231–260. https://doi.org/10.1002/pssb.200301962.

(50) Mohammadbeigi, F.; Kumar, E. S.; Alagha, S.; Anderson, I.; Watkins, S. P. Carbon Related Donor Bound Exciton Transitions in ZnO Nanowires. *J. Appl. Phys.* **2014**, *116* (5), 053516. https://doi.org/10.1063/1.4892090.

(51) Villafuerte, J.; Chaix-Pluchery, O.; Kioseoglou, J.; Donatini, F.; Sarigiannidou, E.; Pernot, J.; Consonni, V. Engineering Nitrogen- and Hydrogen-Related Defects in ZnO Nanowires Using Thermal Annealing. *Phys. Rev. Mater.* **2021**, *5* (5), 056001. https://doi.org/10.1103/PhysRevMaterials.5.056001.

(52) Schirra, M.; Schneider, R.; Reiser, A.; Prinz, G. M.; Feneberg, M.; Biskupek, J.; Kaiser, U.; Krill, C. E.; Thonke, K.; Sauer, R. Stacking Fault Related \$3.31\text{\ensuremath{-}}\mathrm{eV}\$ Luminescence at \$130\text{\ensuremath{-}}\mathrm{meV}\$ Acceptors in Zinc Oxide. *Phys. Rev. B* **2008**, *77* (12), 125215. https://doi.org/10.1103/PhysRevB.77.125215.

(53) Tainoff, D.; Masenelli, B.; Mélinon, P.; Belsky, A.; Ledoux, G.; Amans, D.; Dujardin, C.; Fedorov, N.; Martin, P. Competition between Exciton-Phonon Interaction and Defects States in the 3.31 eV Band in ZnO. *Phys. Rev. B* **2010**, *81* (11), 115304. https://doi.org/10.1103/PhysRevB.81.115304.

(54) Wagner, M. R.; Callsen, G.; Reparaz, J. S.; Schulze, J.-H.; Kirste, R.; Cobet, M.; Ostapenko, I. A.; Rodt, S.; Nenstiel, C.; Kaiser, M.; Hoffmann, A.; Rodina, A. V.; Phillips, M. R.; Lautenschläger, S.; Eisermann, S.; Meyer, B. K. Bound Excitons in ZnO: Structural Defect Complexes versus Shallow Impurity Centers. *Phys. Rev. B* **2011**, *84* (3), 035313. https://doi.org/10.1103/PhysRevB.84.035313.

(55) Cuscó, R.; Alarcón-Lladó, E.; Ibáñez, J.; Artús, L.; Jiménez, J.; Wang, B.; Callahan, M. J. Temperature Dependence of Raman Scattering in ZnO. *Phys. Rev. B* **2007**, *75* (16), 165202. https://doi.org/10.1103/PhysRevB.75.165202.

(56) Noltemeyer, M.; Bertram, F.; Hempel, T.; Bastek, B.; Polyakov, A.; Christen, J.; Brandt, M.; Lorenz, M.; Grundmann, M. Excitonic Transport in ZnO. *J. Mater. Res.* **2012**, *27* (17), 2225–2231. https://doi.org/10.1557/jmr.2012.139.

(57) Gutsche, C.; Niepelt, R.; Gnauck, M.; Lysov, A.; Prost, W.; Ronning, C.; Tegude, F.-J. Direct Determination of Minority Carrier Diffusion Lengths at Axial GaAs Nanowire p–n Junctions. *Nano Lett.* **2012**, *12* (3), 1453–1458. https://doi.org/10.1021/nl204126n.

(58) Gromyko, I.; Krunks, M.; Dedova, T.; Katerski, A.; Klauson, D.; Oja Acik, I. Surface Properties of Sprayed and Electrodeposited ZnO Rod Layers. *Appl. Surf. Sci.* **2017**, *405*, 521–528. https://doi.org/10.1016/j.apsusc.2017.02.065.

For Table of Contents Only